



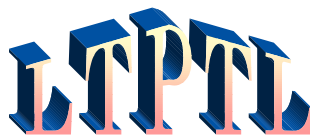
Low Temperature Plasma Technology Laboratory

Superiority of half-wavelength helicon antennas

L. Porte, S.M. Yun, D. Arnush, and F.F. Chen
Electrical Engineering Department

LTP-110

October, 2001



Electrical Engineering Department
Los Angeles, California 90095-1594

Superiority of half-wavelength helicon antennas

L. Porte*, S.M. Yun**, D. Arnush[†], and F.F. Chen^{††}

*Electrical Engineering Department, University of California, Los Angeles
Los Angeles, California 90095-1594*

ABSTRACT

Plasma densities produced by half- and full-wavelength helical antennas in helicon discharges are compared. Contrary to theoretical expectations, half-wavelength antennas are more efficient than full-wavelength ones in producing plasma downstream. This effect is probably caused by capacitive coupling, which interferes with inductive coupling and is not included in the computations.

I. Introduction and definitions

Helicon discharges have been studied intensively because they produce high density plasmas efficiently for use in materials processing, space propulsion, and basic plasma experiments. Helical antennas designed to launch right-hand circularly polarized (azimuthal mode number $m = +1$) helicon waves have previously been found to be more efficient than those of opposite helicity ($m = -1$) or straight ($m = \pm 1$) Nagoya Type III antennas^{1,2}. To further improve antenna coupling, we compared the standard half-wavelength (HW) helical antenna with a full-wavelength (FW) one. Conventional wisdom would indicate that a FW antenna would have a narrower spectrum than a HW antenna with the same wavelength L . If properly designed to match the helicon k -spectrum at the operating plasma density n and dc magnetic field B_0 , where k is the axial wavenumber, the FW antenna should transfer more energy to the plasma than the HW one, resulting in a larger total ion population. Surprisingly, it was found that the opposite was true. The initial measurements were made by the first author (LP) in 1997. To verify the results, the experiment was repeated two years later by the second author (SWY), who found essentially identical results and extended the work by studying the B_0 dependence. In the meantime, the HELIC code³ was developed and improved to give theoretical insight into the behavior of different antennas. However, the issue could not be resolved with this tool, indicating that the behavior of helicon discharges still contains an unknown physical mechanism.

II. Apparatus

Experiments were carried out in the long tube shown in Fig. 1. The field coils provided a uniform B_0 up to 1kG; the gas feed was near the midplane; and the antenna was near one end of the machine, as shown. Unless otherwise specified, the discharge had a fill pressure p of 20 mTorr of argon, with 1.4kW of power P_{rf} at 27.12 MHz and an 800-G field B_0 . Density n , electron temperature KT_e , and space potential V_s were measured with RF-compensated Langmuir probes⁴, the dogleg probe for axial scans and a probe in the port near the midplane for radial scans. Measurements of the wave field components B_z and B_θ were made with a B-dot probe in the same port. The data were reproducible after venting the machine and subsequent pumpdown, even after long periods of inactivity.

Two antennas were compared: a 10-cm long HW antenna (HW10) of 20-cm wavelength, and a 20-cm long FW antenna (FW20) of the same helicity. The HW10 antenna had been found to give the highest densities and had been adopted as the standard. Later, a 15-cm FW antenna (FW15) was also tested, since HELIC computations showed that it gave somewhat higher plasma loading resistance than the 20-cm one. The antennas were constructed of 1-cm wide copper strap. Water cooling of the antennas and the B_0 coils was obviated by operating B_0 in ~ 0.5 sec pulses, and the RF in ~ 10 msec pulses during the flat top. Probe measurements were made during the flat top of the RF pulse, and the RF matchbox was tuned for $<1\%$ reflection before each measurement.

III. Data, Series 1

The radial density profiles with the HW10 and FW20 antennas shown in Fig. 2 are similar and quite normal. The electron temperature is seen to be about 4eV. That helicon waves are launched can be seen from Fig. 3, which shows typical radial profiles of the wave field components B_z and B_θ , together with the simplest Bessel function solutions for these. It is seen that the maxima and minima are approximately in the right positions. Figure 4 shows the axial density profiles obtained with the three antennas under otherwise identical conditions. The HW10 antenna produces much higher downstream density, as well as volume-integrated density, than the FW20 antenna, which is essentially two HW10 antennas laid end-to-end. Note, however, that under the antennas, and in the near-field, the FW20 antenna is superior, as expected *a priori*. The fact that $n(z)$ peaks ~ 50 cm downstream from the antenna was attributed⁵ to pressure balance, followed by radial diffusion loss. That is, as KT_e decays away from the antenna, n must rise to keep nKT_e constant. The force eE_z modifies this condition slightly. Other factors affecting the position of the density peak are ion flow produced at the antenna and downstream ionization. These effects will be discussed later, but they would not be expected to cause a large difference in total ionization when only the length of the antenna is changed.

The plasma loading computed with HELIC for a uniform plasma is shown in Fig. 5. Fig. 5a compares the three antennas in regard to the power absorbed into various plasma modes. The FW15 antenna was chosen because it has the highest peak. However, the total loading resistance shown in Fig. 5b is highest for the FW20 antenna, slightly lower for the FW15 antenna, and lowest for the HW10 antenna. This ordering is reversed in the experimental data, as if the total length of the antenna is more important than matching its helicity with the dominant helicon wavelength.

To see if the plasma conditions differed along the axis for the three cases, other parameters were measured. Fig. 6 shows the variation of KT_e at various position along z . Some differences among the antennas can be seen, but the behavior is not consistent with the density behavior in Fig. 4b. For instance, KT_e for the FW20 antenna falls faster than the others, but there is no corresponding rapid rise in density as pressure balance would require. Fig. 7 shows the wave amplitude vs. z . The characteristic beating⁶ of various radial modes with different k is seen, and the major peaks are in approximate agreement for all cases. The phase of the dominant spectral component vs. z is shown in Fig. 8, clearly showing a propagating wave. The small deviations from linearity of these curves yield measurements of the variation of local wavelength λ ; this is shown in Fig. 9. It is seen that, in the first 40 cm, λ decreases as n rises, in agreement with the helicon dispersion relation. However, all three antennas excite essentially the same waves. None of these measurements yields a clue as to the why the HW10 antenna produces more plasma.

IV. Computations

The parameters used in the following HELIC calculations are: $B_0 = 800$ G, $p = 20$ mTorr, $KT_e = 4$ eV, $f = 27.12$ MHz, and $n_{\text{peak}} = 3.6 \times 10^{13}$ cm⁻³. The radial density profile was taken into account with an analytic fit to the curves in Fig. 2. The k -spectrum of energy absorbed by the plasma at various wavelengths is compared between the HW10 and FW20 antennas in Fig. 10. This is a superposition of the plasma response and the k -spectrum of the antenna, shown by the respective curves. In spite of the fact that the FW20 antenna does not match the plasma resonances as well as does the HW10 antenna, the total loading is much higher for the FW20. Note that neither antenna has its peak response matching the wavelength of the coil, whose k value is marked by the vertical line. Apparently, the end rings have an appreciable effect on the antenna spectrum. The two antennas' end rings differ not only by their separation, but also in the relative direction of the currents in them². Surprisingly, the $P(k)$ spectra of FW and HW antennas of the same length are similar in shape, with the FW spectrum higher; the pitch of the winding does not appear to matter.

Axial power deposition profiles for the three antennas are shown in Fig. 11. In each case, the current in the antenna was assumed to be 1A; the FW15 antenna was the most efficient in this case. In the neighborhood of $z = 50$ cm, where the HW10 antenna gives a density peak, the absorption is 13% of the maximum, even when the decay in KT_e has been neglected. Therefore, downstream ionization is not likely to contribute to the dominance of the HW10 antenna in that region. Distribution of power absorbed over radius is shown in Fig. 12 for the HW10 and FW20 antennas. It was thought that perhaps most of the FW power was deposited near the edge, where the plasma created is more easily lost than if created near the axis. However, it is seen that, if anything, the FW antenna had more central deposition. When the volume at each radius is taken into account, the bottom curves in Fig. 12 show that most of the power is deposited near the edge, as would be expected³ at 800G because of coupling to the Trivelpiece-Gould (TG) modes. The dominance of edge deposition may vary, however, with axial position. The $P(r)$ profiles *not* integrated over z are shown in Fig. 13. There is some variation with z , but in no case is much power absorbed in the central region.

Since the antenna windings have $m = 1$ symmetry, they couple primarily to $m = 1$ helicon waves. However, since the antenna has finite length, coupling to other odd m -numbers is also possible. The loading by $m = 3$ and 5 modes is shown for the FW20 antenna in Fig. 14. It is seen that the coupling falls rapidly with m , and $m > 1$ adds little to the total absorption. This is even more true for the HW10 case.

Of the effects that are not included in the HELIC code, these are the most obvious: (1) *Axial gradients in n and KT_e* . As seen in Fig. 6, there does not appear to be a difference in $T_e(z)$ for the HW10 and FW20 antennas that could give higher downstream density for the former. (2) *Ionization by non-Maxwellian electron populations*. An ionizing electron of, say, 50 eV would have a mean-free path of ~ 10 cm, dominated by neutral collisions at 10 mTorr. It is not likely for these to reach the density peak at $z = 50$ cm. However, if neutral depletion lowers the central pressure to 2 mTorr, then it would be possible for Landau damping of helicon waves to produce a few of such electrons. Attempts⁷ to detect fast electrons in our laboratory have yielded an upper limit of 10^{-4} of the total density. In any case, the FW antenna, with its purer spectrum, should produce more of these electrons than the HW antenna. (3) *Ion flow out of the antenna region*. If there is little downstream ionization, ions leaving the antenna should be uni-directional. In that case, the Bohm criterion for monotonic sheath formation should obtain, and the ions must stream out with the ion acoustic velocity. This effect has been inferred previously⁸. The ion momentum then carries the

plasma downstream, raising the density there over that in the static case. This effect would, however be the same for both HW and FW antennas. (4) *Radial transport*. HELIC is not a diffusion code, and the possibility of a difference in diffusion will be raised in the next section.

V. Data, Series 2

The following measurements were made in the same apparatus two years later with a 5-cm long HW antenna and a 10-cm long FW antenna. The variation of n with B_0 is shown in Fig. 15. Density jumps at critical fields, typical of helicon discharges, are seen with both antennas. Also seen is a small density peak near 50G, another helicon characteristic. A third well-known effect is the much lower density produced when the antenna helicity is reversed to match the $m = -1$ mode. Fig. 16 shows axial density profiles at different fields B_0 . At high B_0 , the dominance of the HW antenna shown in Fig. 4 is reproduced. At low B_0 , below the density jumps, the FW antenna produces higher n . Radial density profiles are shown in Fig. 17 for six values of B_0 . At 100G and below, both antennas are inefficient, but the FW antenna is somewhat better. The HW antenna causes a density jump before the FW one does (*cf.* Fig. 15), and at 200G the HW antenna is superior. It continues to dominate up to the highest field of 800G. Note that at fields beyond the density jump the profiles assume a “triangular” shape, which has been explained by ion-electron dominated collisions together with a TG-mode absorption profile⁹.

The density data confirm the superiority of the HW antenna seen in the data of Series 1 but do not provide an explanation. More light on the problem is provided by measurements of the antenna loading vs. B_0 . Figure 18 shows that, above 200G, both the voltage and current applied to the FW antenna are higher than to the HW antenna. When the phases are accounted for, one obtains in Fig. 19 the resistance R and reactance $|X|$ seen by the antennas. These are considerably higher for the FW antenna than for the HW antenna. The higher voltage on the FW antenna is expected because of its longer length, and hence higher inductance. Its higher loading resistance agrees with the HELIC results shown in Sec. IV, but it should result in higher density, not lower. R vs. P_{rf} is shown in Fig. 20, together with n . The HW antenna has its density jump at much lower power than does the FW antenna, presumably because its spectrum matches the plasma modes better (*cf.* Fig. 10). Moreover, it yields higher density at all P_{rf} , even though R is smaller at all P_{rf} . Computed curves of $P(k)$ and $P(z)$ are similar to those in Figs. 10 and 11, except that the HW5/FW20 coupling ratio is expected to be even smaller than the HW10/FW20 ratio, contrary to the experimental results.

Fig. 21 shows radial profiles of space potential for the two antennas. These profiles would be low in the center if electrons were magnetically confined, and they would be peaked in the center if the electrons obeyed the Boltzmann relation and followed the shape of the density profile. The latter occurs in short machines where electrons can cross field lines via the short-circuit effect at the endplate sheaths. The fact that $V_s(r)$ is essentially flat in the body of the discharge means that the machine length achieves a balance between these two effects. The important point to notice in Fig. 21 is that V_s is higher for the FW antenna. This would cause ions to be lost radially faster than for the HW antenna, while electrons can follow the ions by the partial short-circuit effect. It is reasonable for V_s to be higher for the FW antenna because the applied voltage is higher, and capacitive coupling is more effective. This would cause large RF oscillations at the edge which the electrons can follow but the ions cannot, because of the high frequency. The θ -component of the capacitive electric field would cause radial oscillations of the electron guiding centers, causing an enhanced electron loss at the edge, raising the plasma potential. Evidence of these oscillation is seen in Fig. 22,

which shows peak-to-peak amplitudes of floating potential oscillations *vs.* B_0 . Below the critical field of $\sim 150\text{G}$ where the density jump occurs, the discharge is capacitively coupled, and the HW antenna causes larger oscillations because of its higher impedance. At high fields, there is some evidence that the HW antenna causes larger edge oscillations even in the inductively coupled region. This raises the possibility that the FW antenna suffers from faster plasma loss because a larger fraction of the power is capacitively coupled.

VI. Conclusions

In two separate experiments, half-wavelength, right-hand helical antennas have been found to produce higher downstream density and more total ionization than full wavelength antennas of the same helicity. Detailed calculations based on inductive coupling to helicon-TG waves predict the opposite; namely, that rf absorption should be higher for FW than for HW antennas. It is conjectured that the discrepancy is caused by capacitive coupling, which interferes with inductive coupling and enhances the radial loss of plasma to the walls. Measurements of space potential and potential oscillations lend credence to this supposition.

FIGURE CAPTIONS

Fig. 1. Diagram of the apparatus.

Fig. 2. Radial density profiles 26 cm downstream from antenna midplane for the 10-cm HW (■) and 20-cm FW (●) antennas. Data from both sides of the axis have been averaged to produce symmetric curves. The electron temperature (Δ) was measured with the HW antenna.

Fig. 3. Typical radial profiles of the wave magnetic field components $|B_z|$ and $|B_\theta|$. Data from both sides of the axis have been averaged to produce symmetric curves. The solid lines are simple Bessel function fits.

Fig. 4. Axial variation of density produced by the HW10 (■), FW15 (○), and FW20 (◆) antennas. The lengths and locations of the antennas are shown at the lower left corner. (a) and (b) are two sets of data taken months apart, showing reproducibility.

Fig. 5. (a) RF absorption per unit k vs. helicon wavelength for the FW20, FW15, and HW10 antennas. (b) Total plasma loading vs. antenna length for FW and HW antennas. The three antennas used are marked with arrows.

Fig. 6. Axial variation of electron temperature with the three antennas, corresponding to the run of Fig. 4b. The rise in KT_e for the FW20 antenna at large z is caused by failure of RF compensation at low densities.

Fig. 7. Wave amplitude $|B_z|$ vs. z excited by the three antennas.

Fig. 8. Phase of B_z oscillations vs. axial position.

Fig. 9. Local wavelength vs. z for the three antennas. The anomaly at $z > 60$ cm for the FW20 antenna is caused by the weak signal there.

Fig. 10. Computed k -spectra of energy deposition by the FW20 (●) and HW10 (■) antennas under the experimental conditions. The lines are the k -spectra of the antennas in vacuum. The vertical line marks the k of the antenna winding.

Fig. 11. Calculated axial power deposition profiles for three antennas, integrated over the cross section. Conditions were: $B_0 = 800\text{G}$, $p = 10\text{mTorr}$, and $KT_e = 4\text{eV}$, all uniform. The density was uniform along z but had the experimental radial profile with $n_{\text{peak}} = 3.6 \times 10^{13} \text{cm}^{-3}$.

Fig. 12. Calculated radial power deposition profiles for three antennas for the same conditions as in Fig. 11. The curves are integrated over all z . The points are $P(r)$, and the lines are proportional to $2\pi rP(r)$.

Fig. 13. Comparison of radial power deposition profiles for the HW10 and FW20 antennas at the same z [(b) and (c)], and at the respective antenna ends [(a) and (c)].

Fig. 14. k -spectrum of power absorbed by the FW20 antenna into helicon modes of various azimuthal mode numbers m .

Fig. 15. Density vs. magnetic field at $r = 2$ cm, $z = 24$ cm with HW5 and FW10 antennas at 857W and 10mTorr of Ar. The $m = -1$ mode is excited by reversing the direction of B_0 .

Fig. 16. Axial density profiles with the HW5 (squares) and FW10 (circles) antennas at three magnetic fields.

Fig. 17. Radial density profiles at $z = 24$ cm at various B_0 with the HW (squares) and FW (circles) antennas.

Fig. 18. Magnitudes of RF voltage (solid points) and current (open points, RH scale) applied to the HW (squares) and FW (circles) antennas.

Fig. 19. Magnitudes of loading resistance (solid points) and reactance (open points) presented by the plasma to the HW (squares) and FW (circles) antennas.

Fig. 20. Density (solid points) and loading resistance (open points) vs. RF power for the HW (squares) and FW (circles) antennas.

Fig. 21. Plasma potential vs. radius at 800G, $z = 48$ cm for the FW (●) and HW (■) antennas.

Fig. 22. Peak-to-peak oscillation amplitude in floating potential vs. B_0 at $z = 24$ cm, $r = 1.5$ cm for the two antennas.

REFERENCES

* Electronic address: laurieporte@hotmail.com

** Electronic address: seokmin.yun@lamrc.com

† Electronic address: darnush@ucla.edu

†† Electronic address: ffchen@ee.ucla.edu

¹ F.F. Chen, J. Vac. Sci. Technol. A **10**, 1389 (1992).

² D.G. Miljak and F.F. Chen, Plasma Sources Sci. Technol. **7**, 61 (1998).

³ D. Arnush, Phys. Plasmas **7**, 3042 (2000).

⁴ I.D. Sudit and F.F. Chen, Plasma Sources Sci. Technol. **3**, 162 (1994).

⁵ I.D. Sudit and F.F. Chen, Plasma Sources Sci. Technol. **5**, 43 (1996).

⁶ M. Light, I.D. Sudit, F.F. Chen, and D. Arnush, Phys. Plasmas **2**, 4094 (1995).

⁷ F.F. Chen and D.D. Blackwell, Phys. Rev. Lett. **82**, 2677 (1999).

⁸ G.R. Tynan, A.D. Bailey III, G.A. Campbell, R. Charatan, A. de Chambrier, G. Gibson, D.J. Hemker, K. Jones, A. Kuthi, C. Lee, T. Shoji, and M. Wilcoxson, J. Vac. Sci. Technol. A **15**, 2885 (1997).

⁹ F.F. Chen, Plasma Sources Sci. Technol. **7**, 458 (1998).

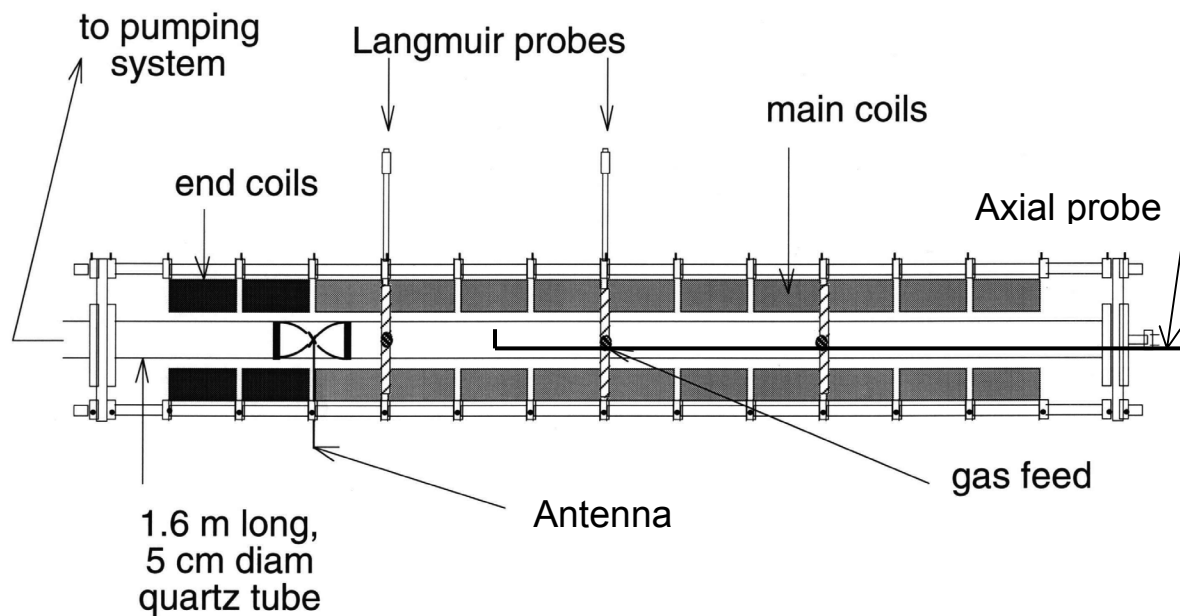


Fig. 1. Diagram of the apparatus.

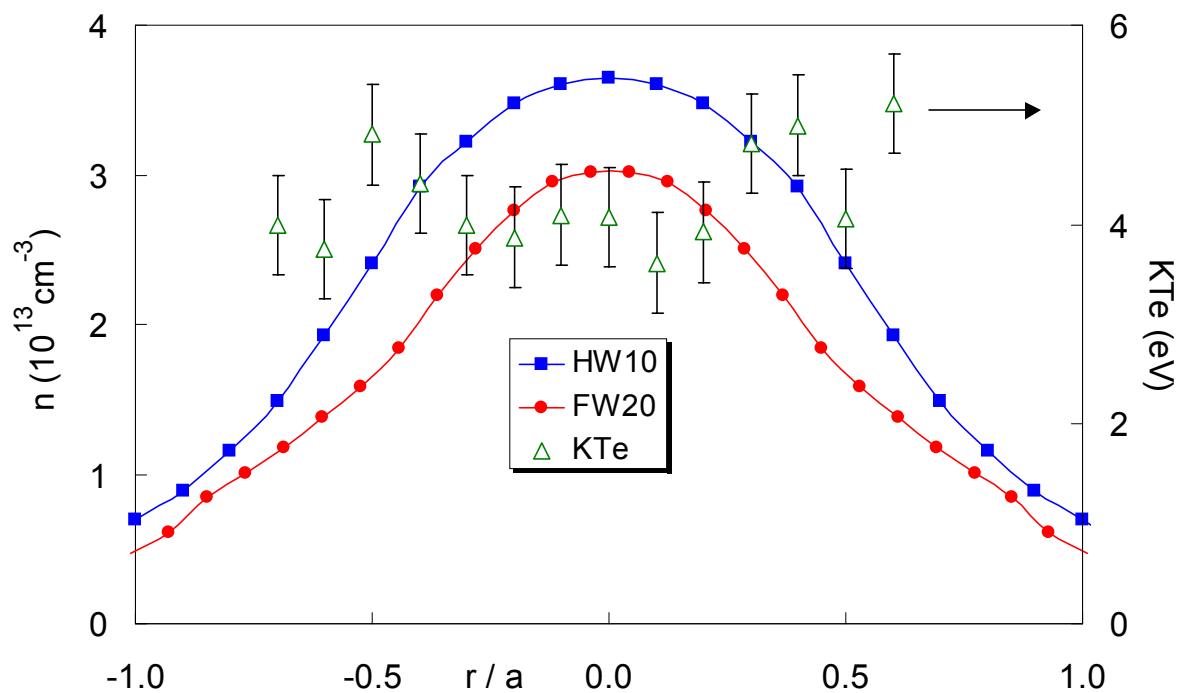


Fig. 2. Radial density profiles 26 cm downstream from antenna midplane for the 10-cm HW (■) and 20-cm FW (●) antennas. Data from both sides of the axis have been averaged to produce symmetric curves. The electron temperature (Δ) was measured with the HW antenna.

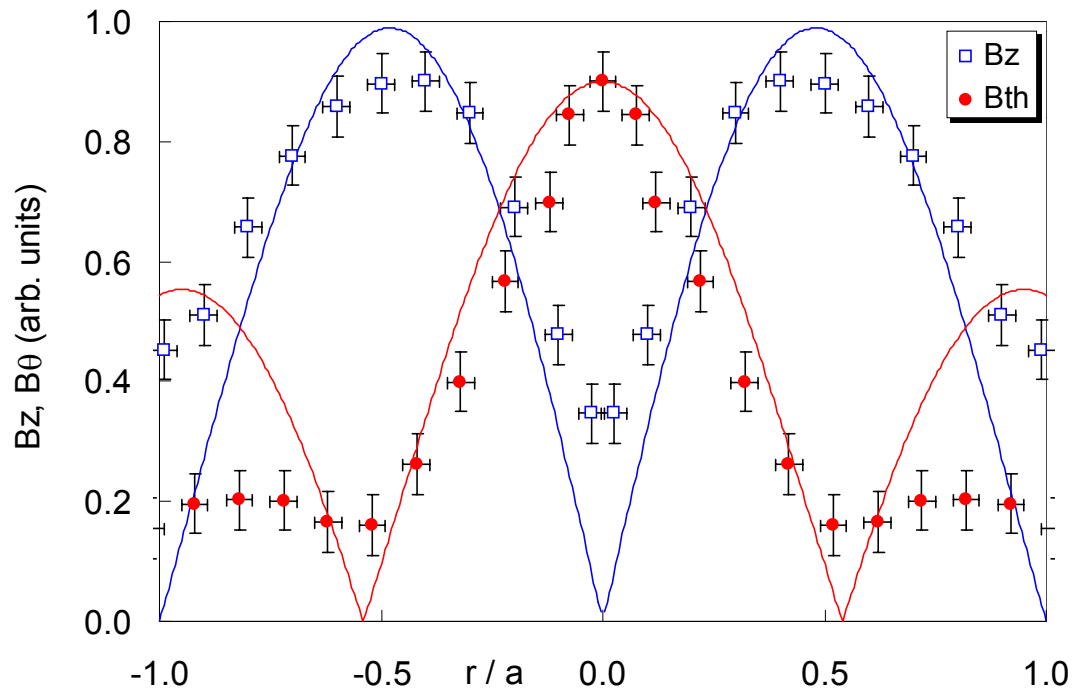


Fig. 3. Typical radial profiles of the wave magnetic field components $|B_z|$ and $|B_\theta|$. Data from both sides of the axis have been averaged to produce symmetric curves. The solid lines are simple Bessel function fits.

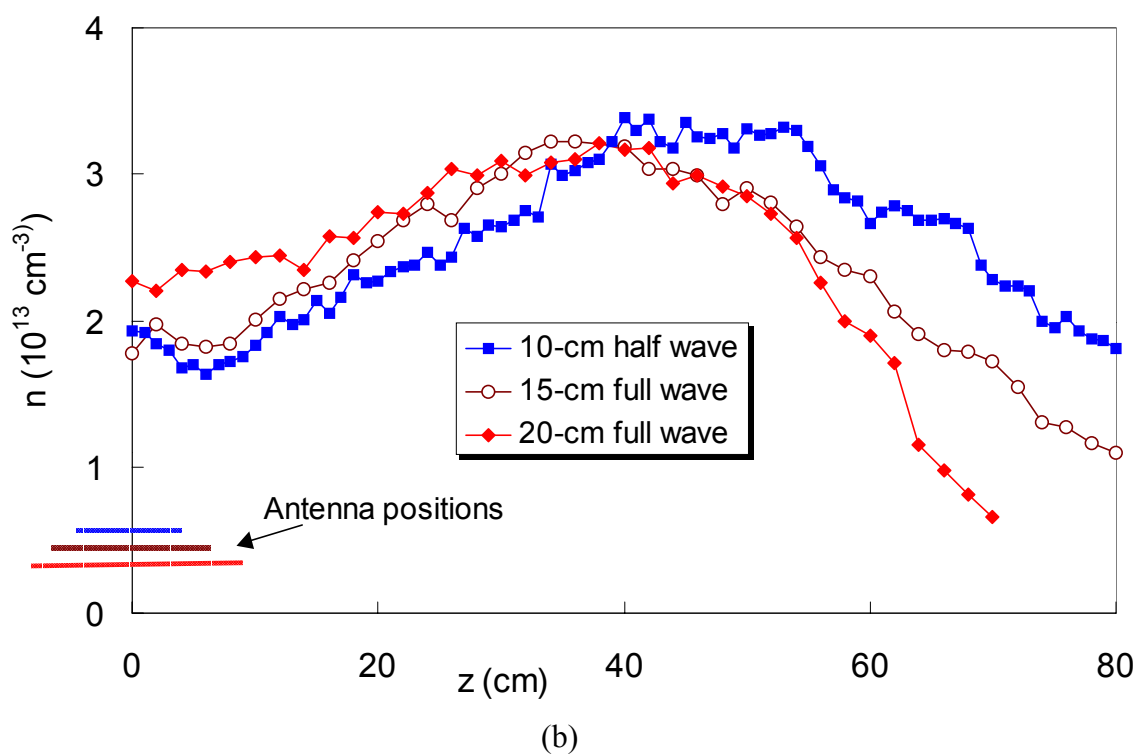
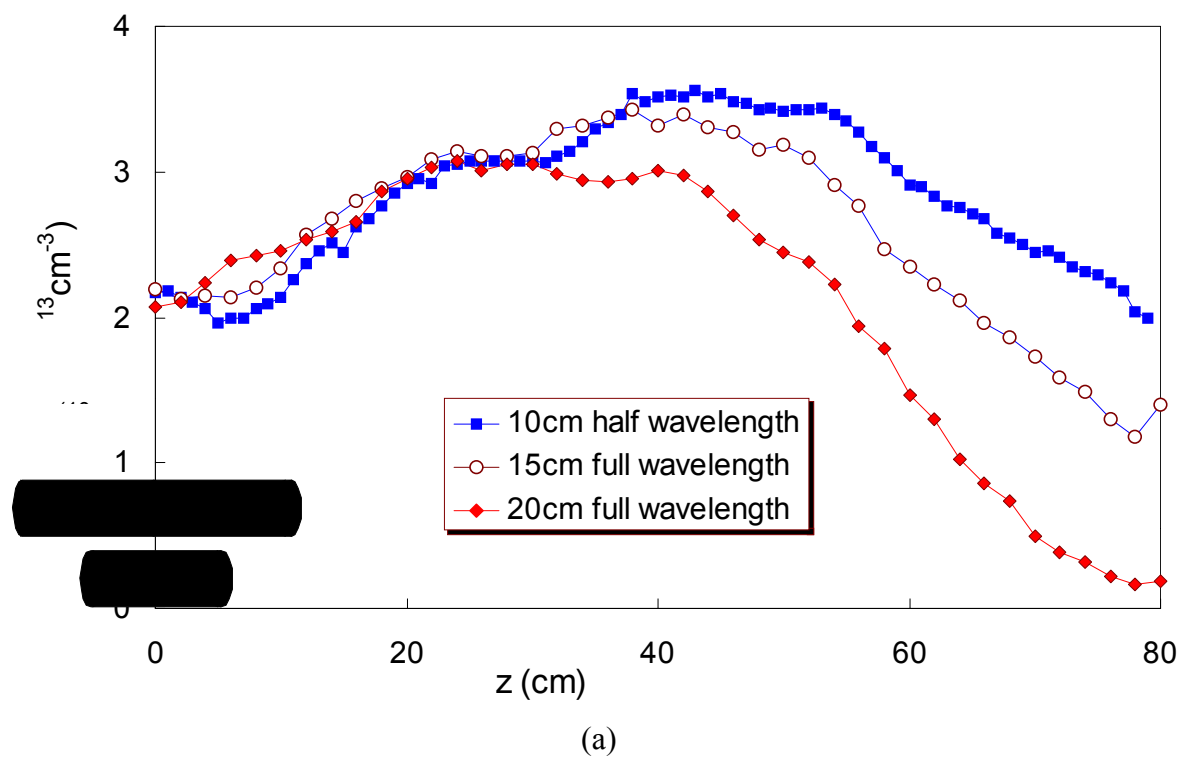
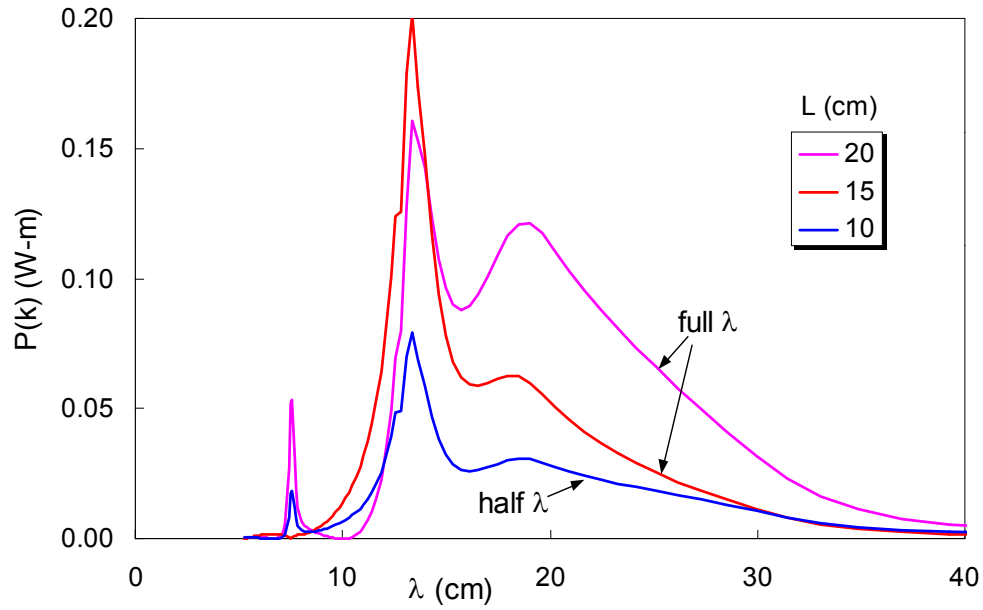
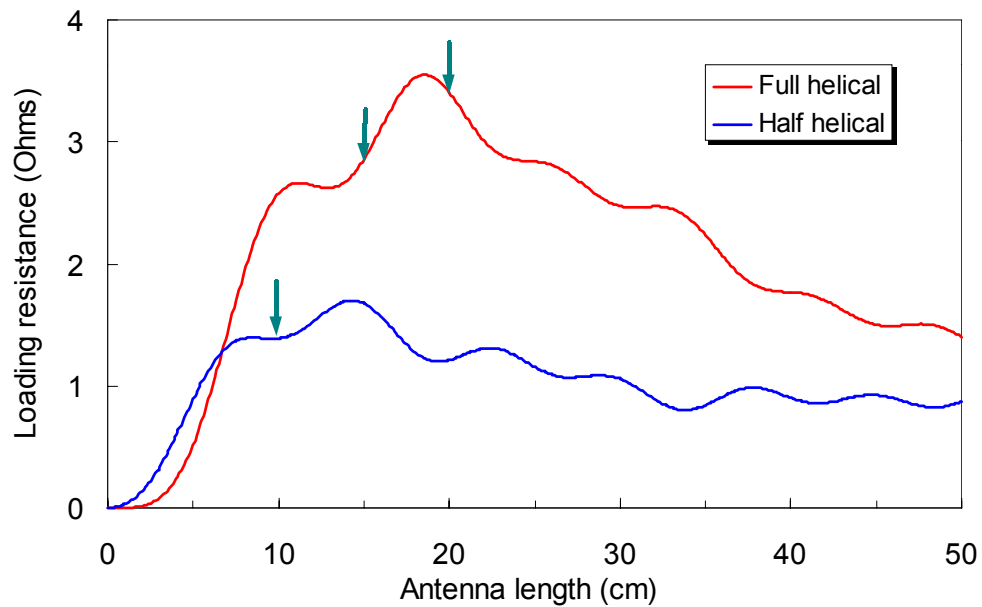


Fig. 4. Axial variation of density produced by the HW10 (■), FW15 (○), and FW20 (◆) antennas. The lengths and locations of the antennas are shown at the lower left corner. (a) and (b) are two sets of data taken months apart, showing reproducibility.



(a)



(b)

Fig. 5. (a) RF absorption per unit k vs. helicon wavelength for the FW20, FW15, and HW10 antennas. (b) Total plasma loading vs. antenna length for FW and HW antennas. The three antennas used are marked with arrows.

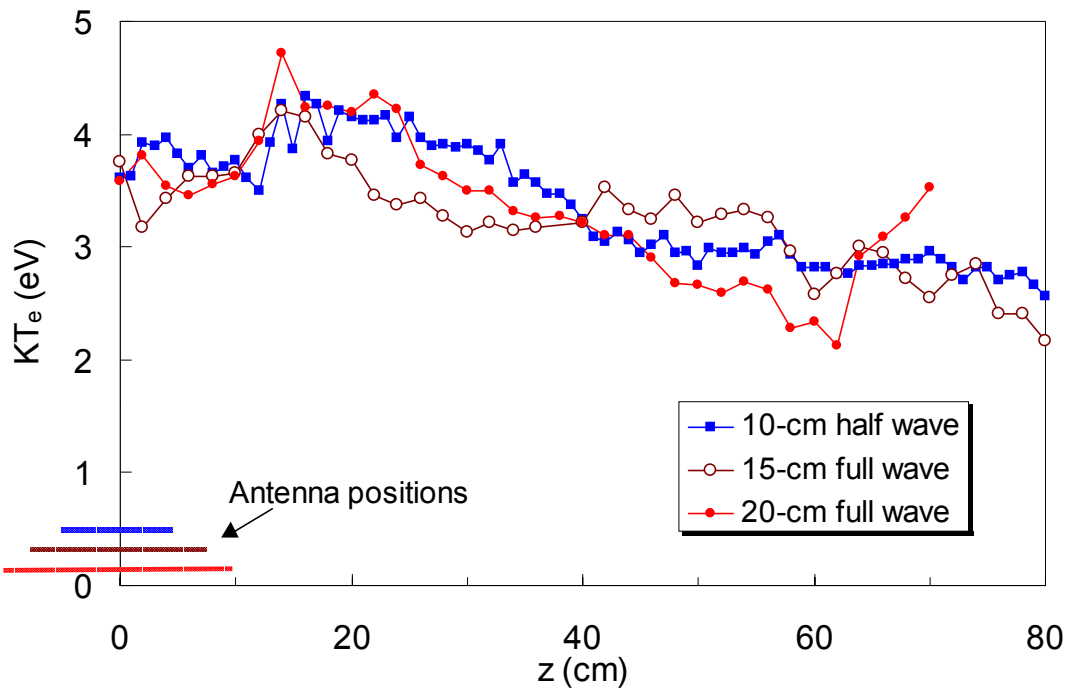


Fig. 6. Axial variation of electron temperature with the three antennas, corresponding to the run of Fig. 4b. The rise in KT_e for the FW20 antenna at large z is caused by failure of RF compensation at low densities.

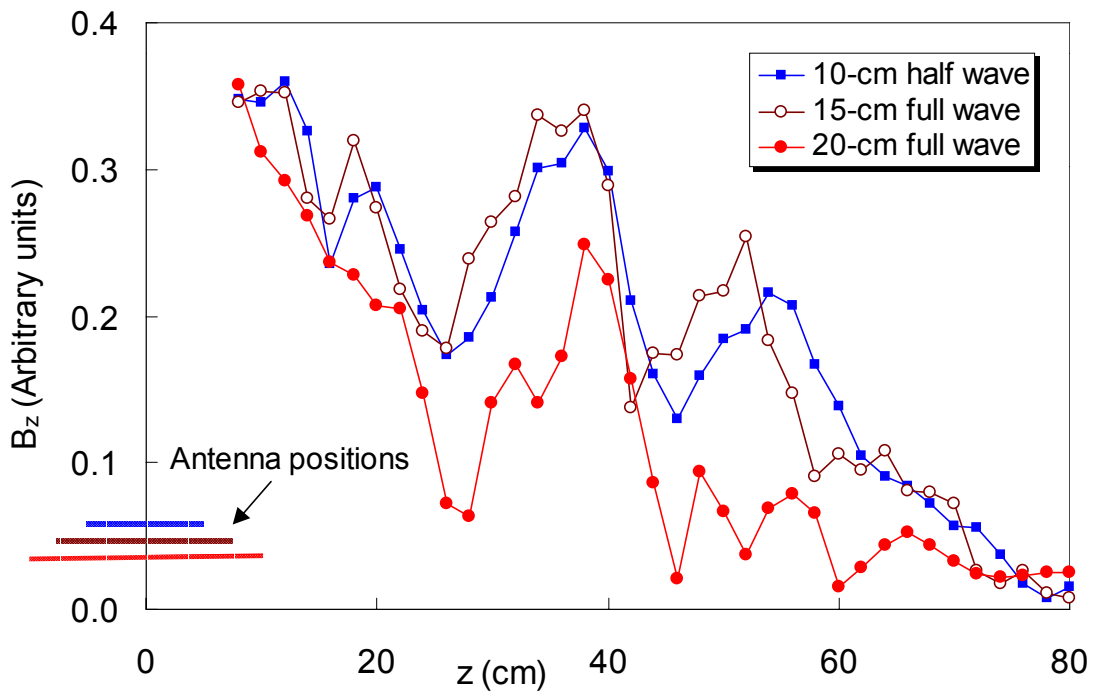


Fig. 7. Wave amplitude $|B_z|$ vs. z excited by the three antennas.

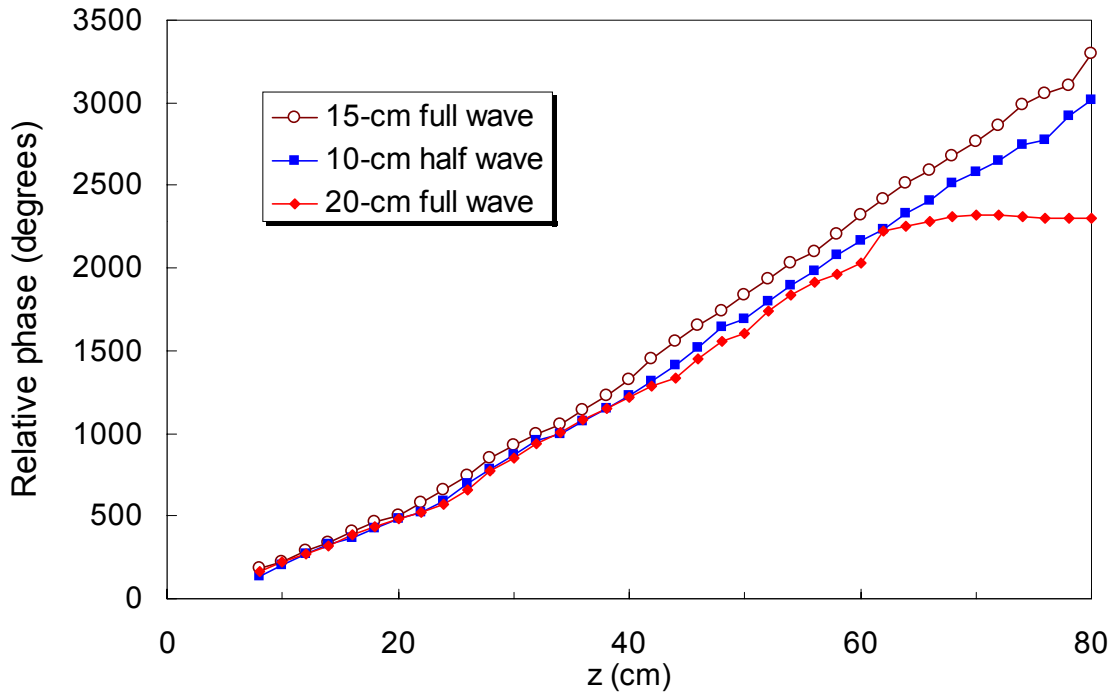


Fig. 8. Phase of B_z oscillations vs. axial position.

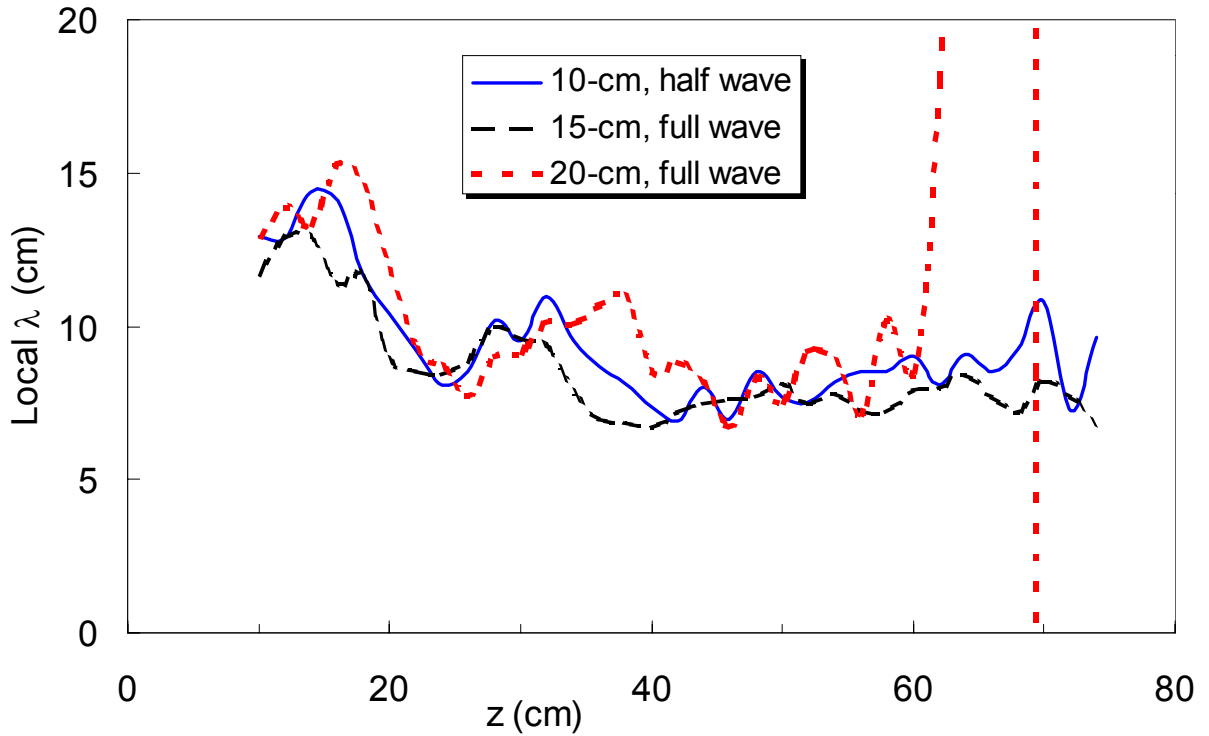


Fig. 9. Local wavelength vs. z for the three antennas. The anomaly at $z > 60$ cm for the FW20 antenna is caused by the weak signal there.

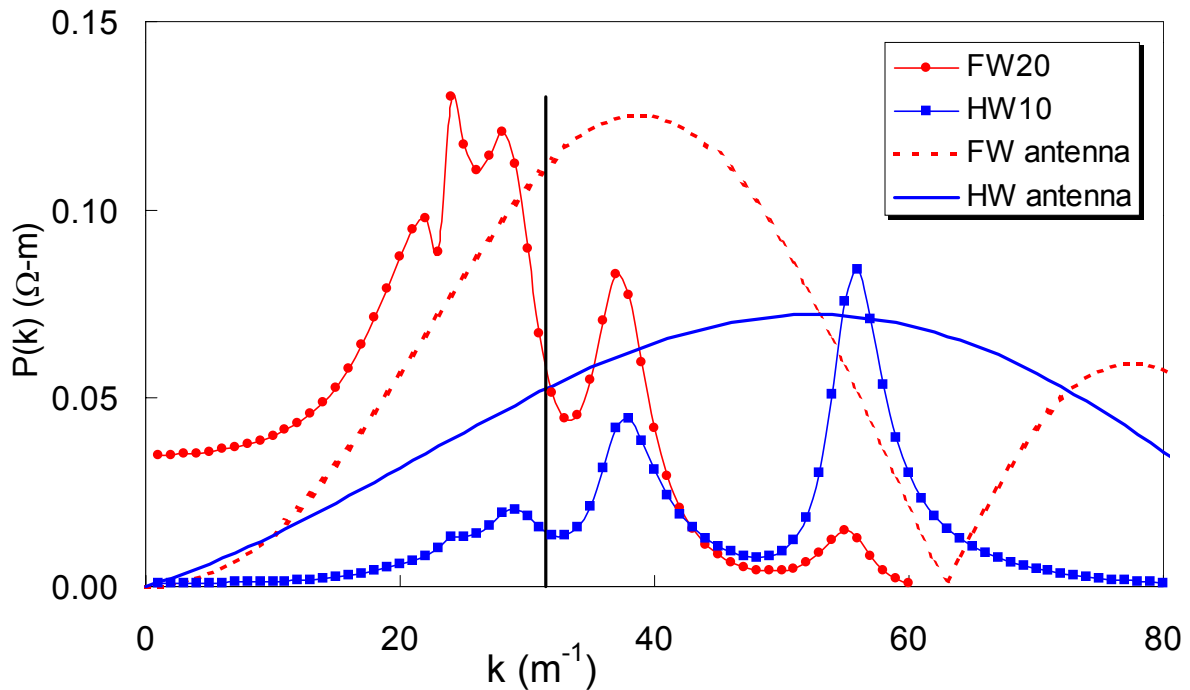


Fig. 10. Computed k -spectra of energy deposition by the FW20 (●) and HW10 (■) antennas under the experimental conditions. The lines are the k -spectra of the antennas in vacuum. The vertical line marks the k of the antenna winding.

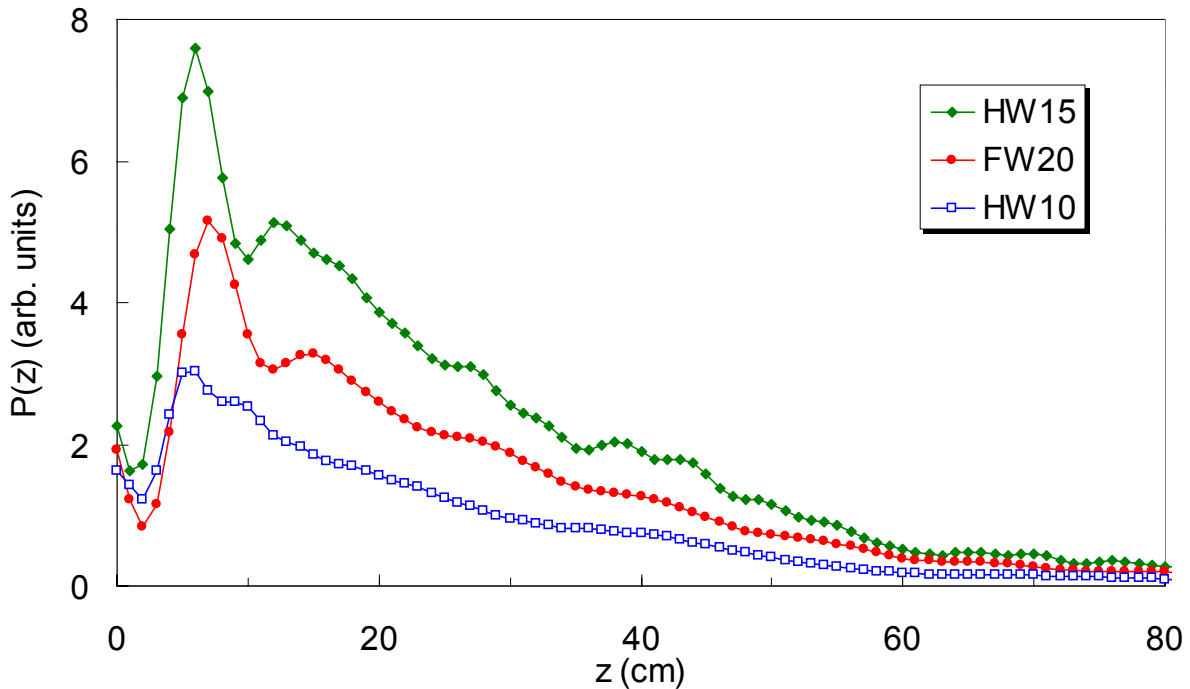


Fig. 11. Calculated axial power deposition profiles for three antennas, integrated over the cross section. Conditions were: $B_0 = 800\text{G}$, $p = 10\text{mTorr}$, and $KT_e = 4\text{eV}$, all uniform. The density was uniform along z but had the experimental radial profile with $n_{\text{peak}} = 3.6 \times 10^{13} \text{cm}^{-3}$.

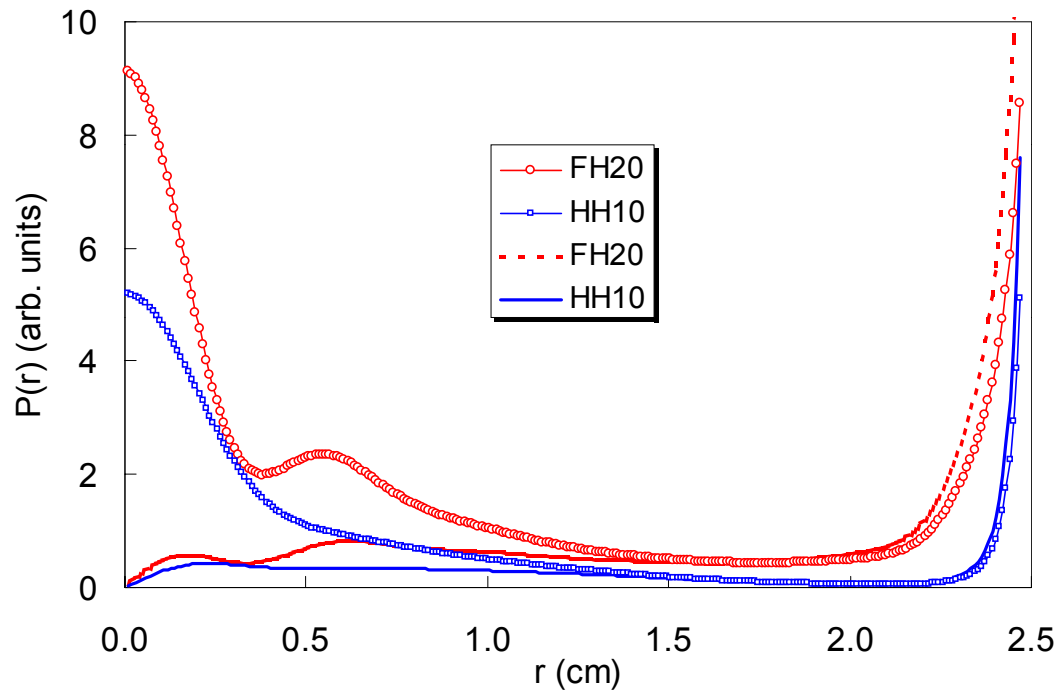


Fig. 12. Calculated radial power deposition profiles for three antennas for the same conditions as in Fig. 11. The curves are integrated over all z . The points are $P(r)$, and the lines are proportional to $2\pi rP(r)$.

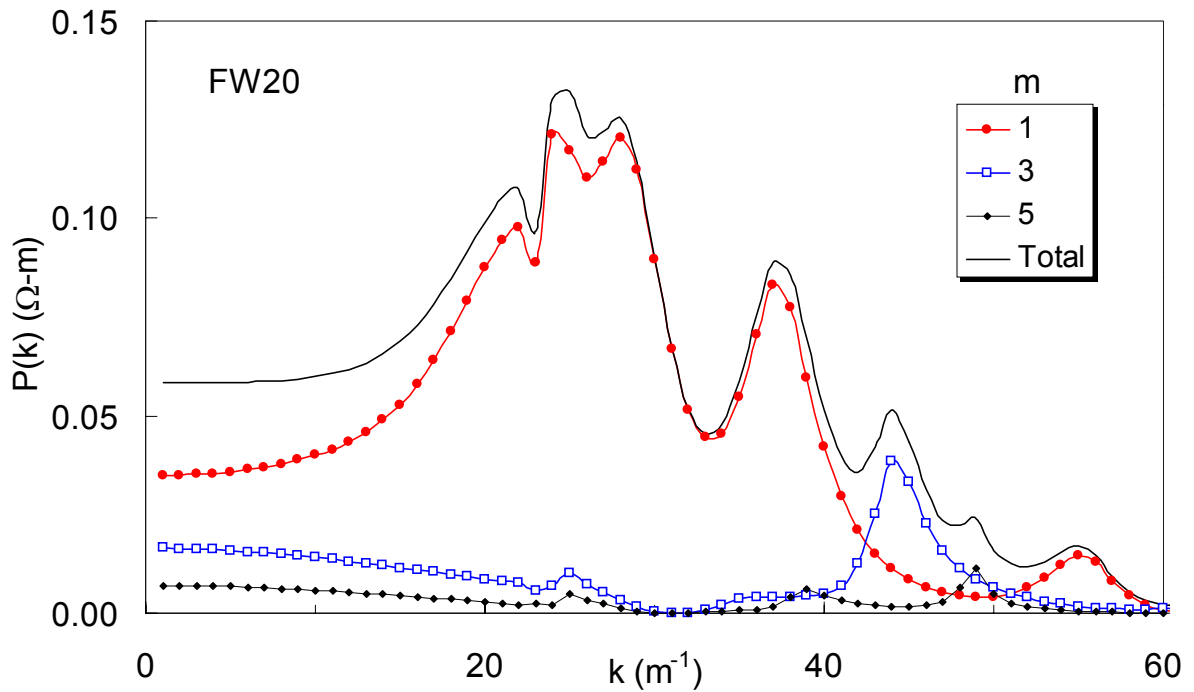


Fig. 14. k -spectrum of power absorbed by the FW20 antenna into helicon modes of various azimuthal mode numbers m .

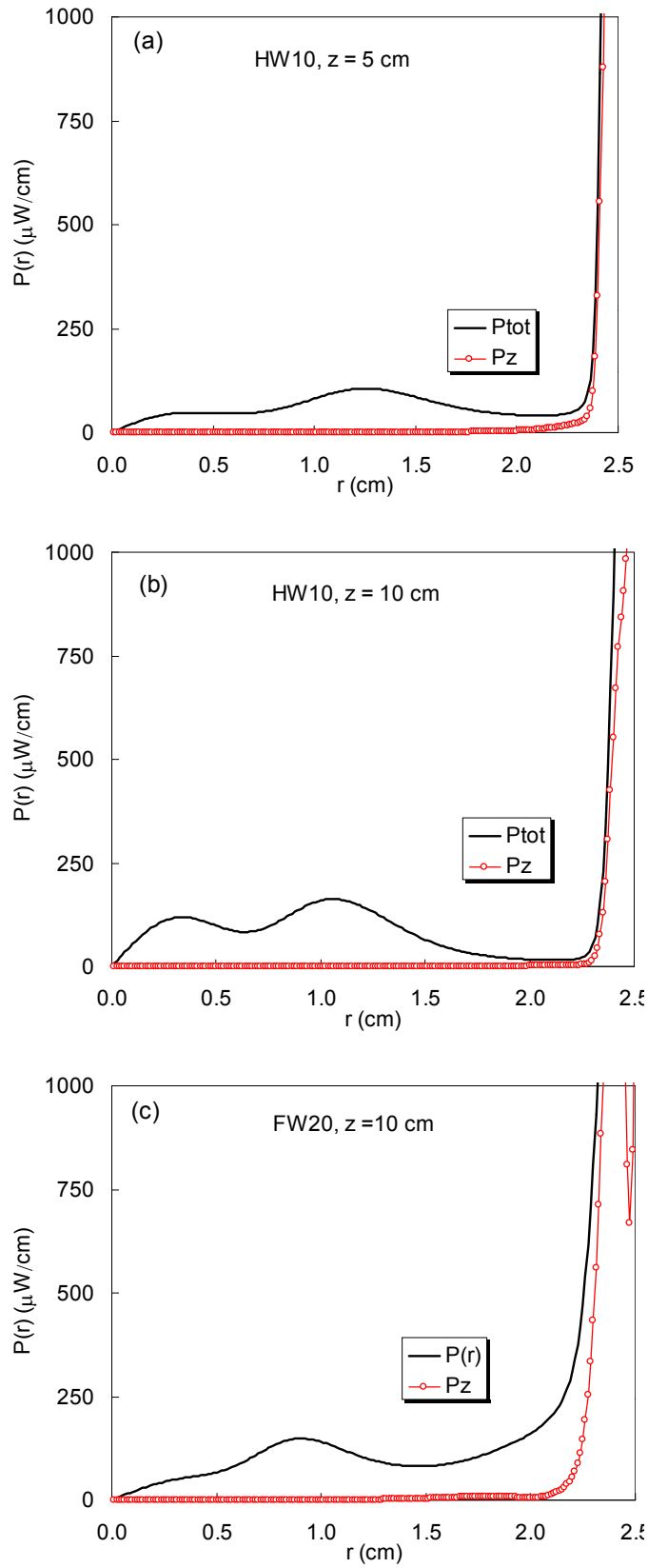


Fig. 13. Comparison of radial power deposition profiles for the HW10 and FW20 antennas at the same z [(b) and (c)], and at the respective antenna ends [(a) and (c)].

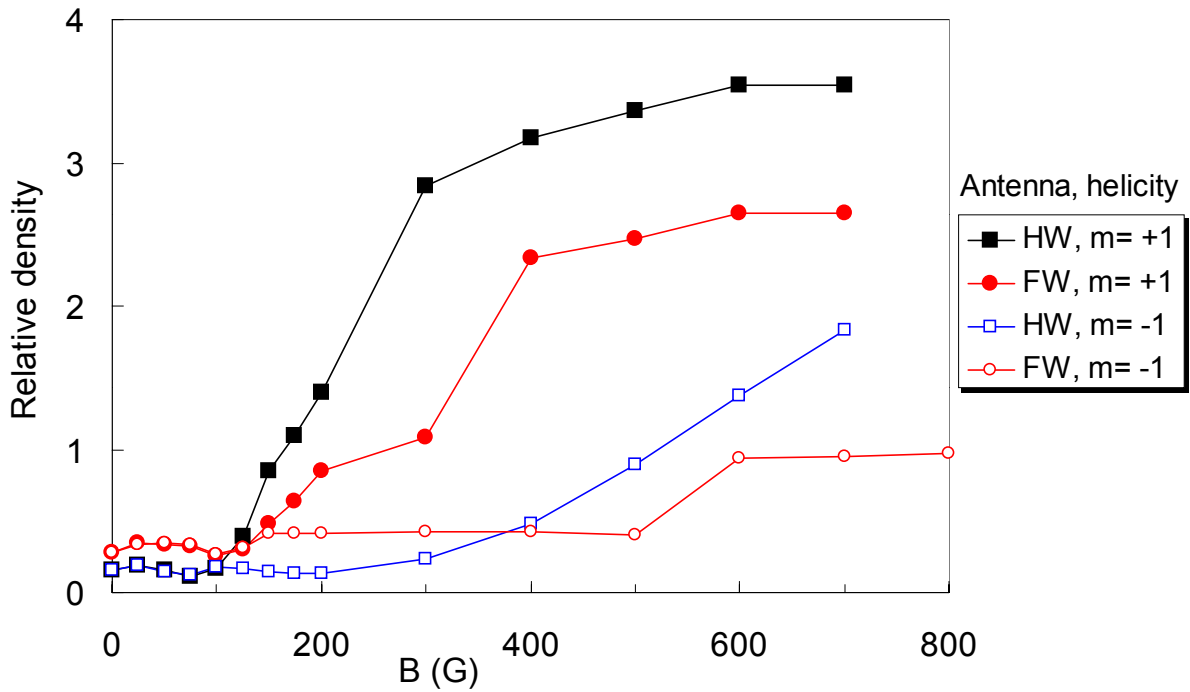


Fig. 15. Density vs. magnetic field at $r = 2$ cm, $z = 24$ cm with HW5 and FW10 antennas at 857W and 10mTorr of Ar. The $m = -1$ mode is excited by reversing the direction of B_0 .

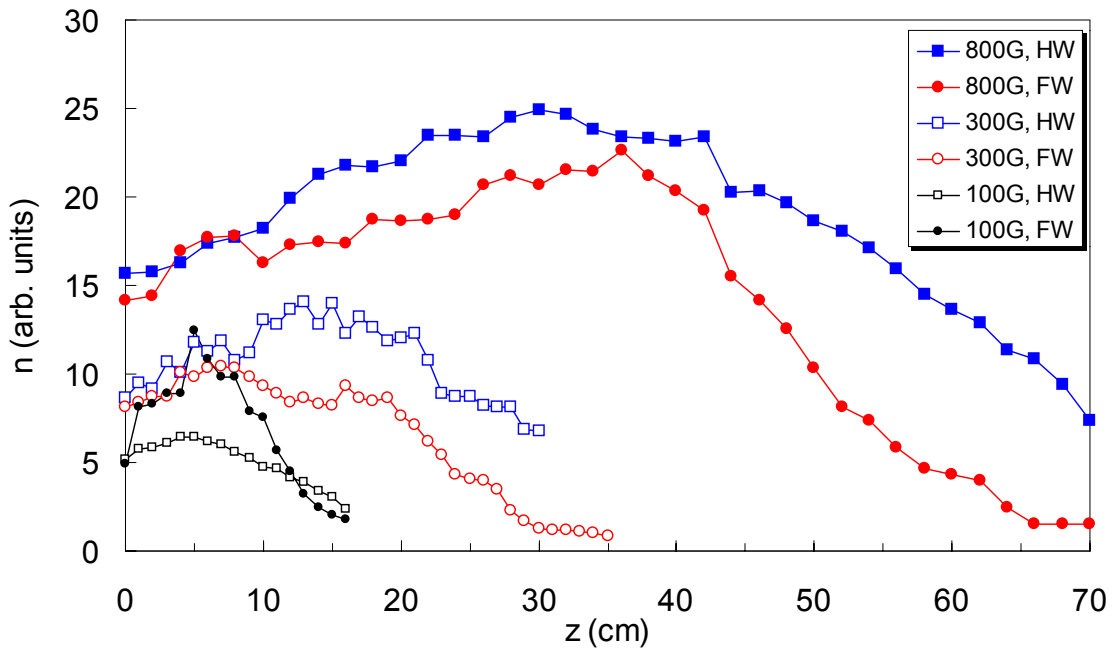


Fig. 16. Axial density profiles with the HW5 (squares) and FW10 (circles) antennas at three magnetic fields.

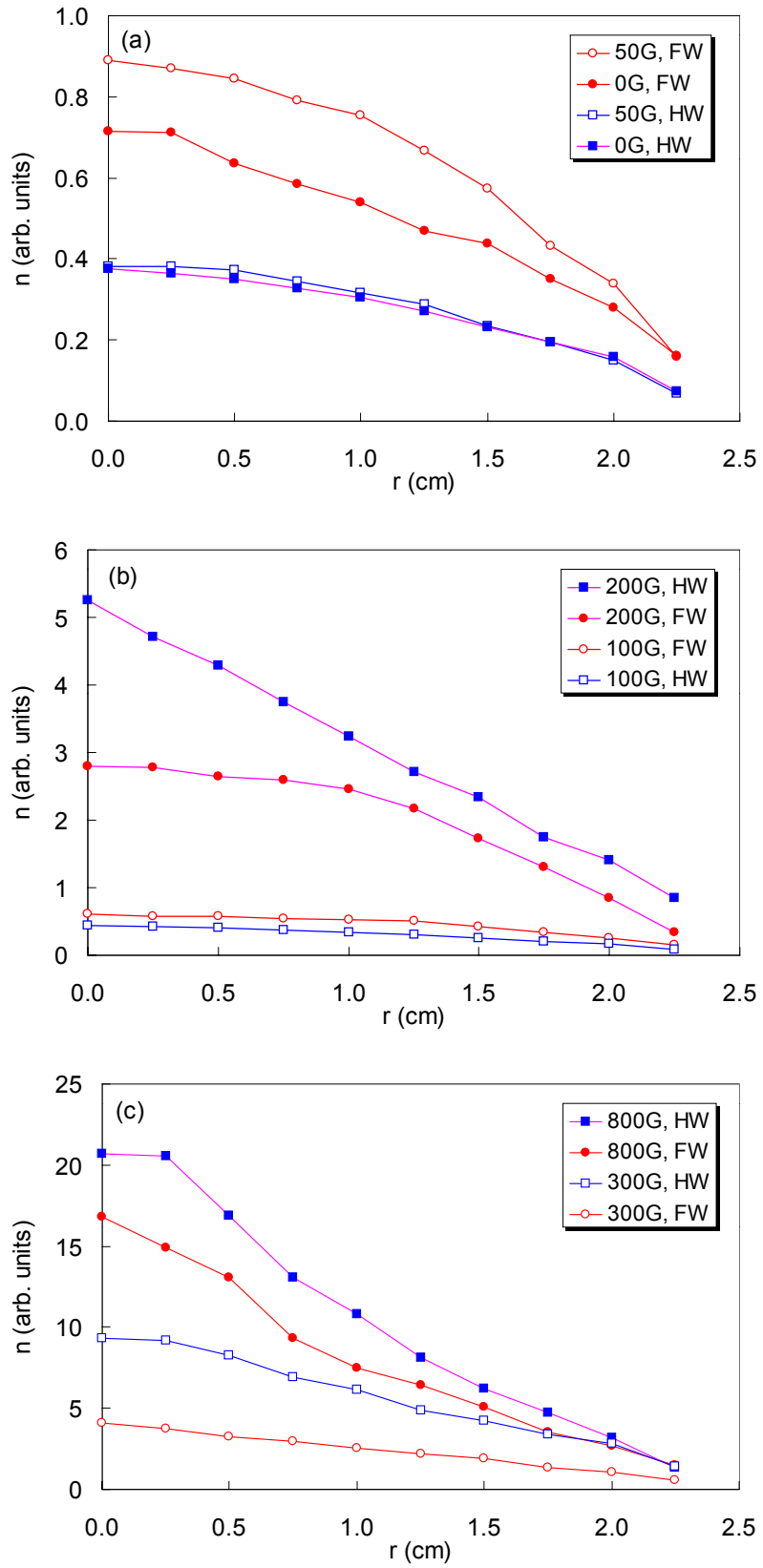


Fig. 17. Radial density profiles at $z = 24$ cm at various B_0 with the HW (squares) and FW (circles) antennas.

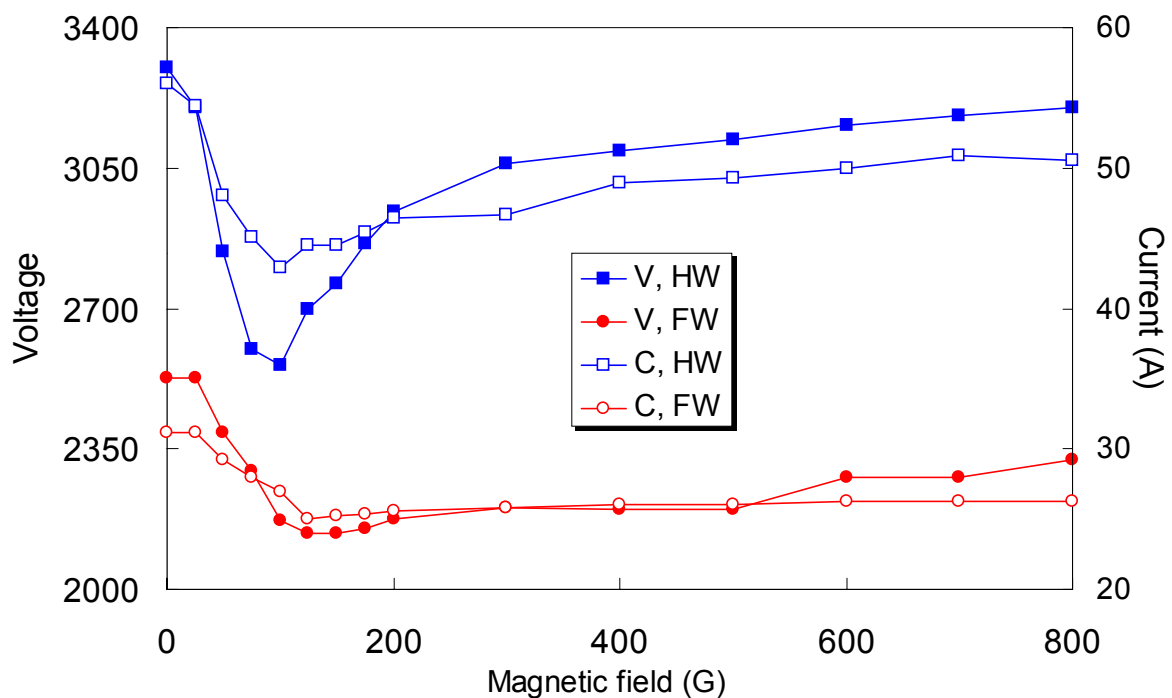


Fig. 18. Magnitudes of RF voltage (solid points) and current (open points, RH scale) applied to the HW (squares) and FW (circles) antennas.

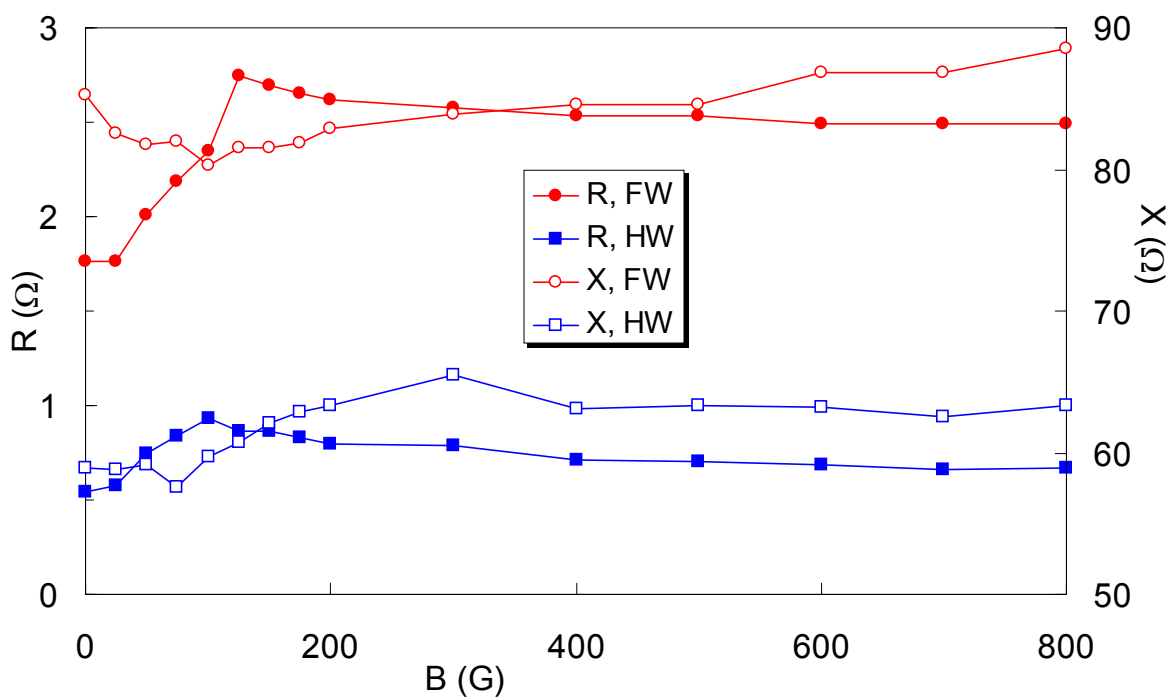


Fig. 19. Magnitudes of loading resistance (solid points) and reactance (open points) presented by the plasma to the HW (squares) and FW (circles) antennas.

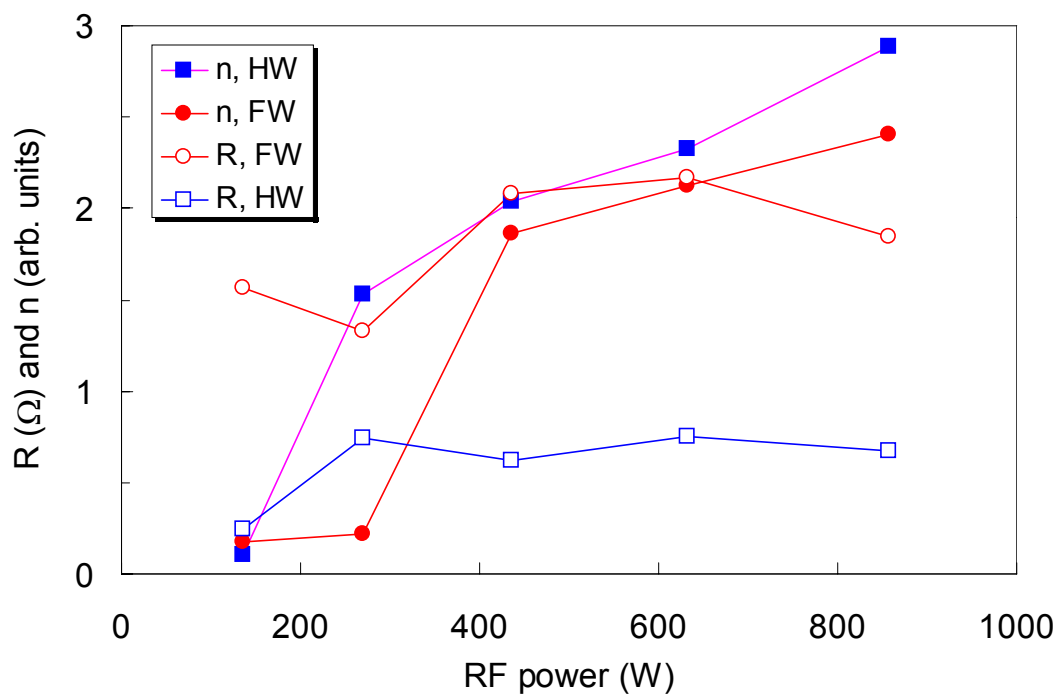


Fig. 20. Density (solid points) and loading resistance (open points) vs. RF power for the HW (squares) and FW (circles) antennas.

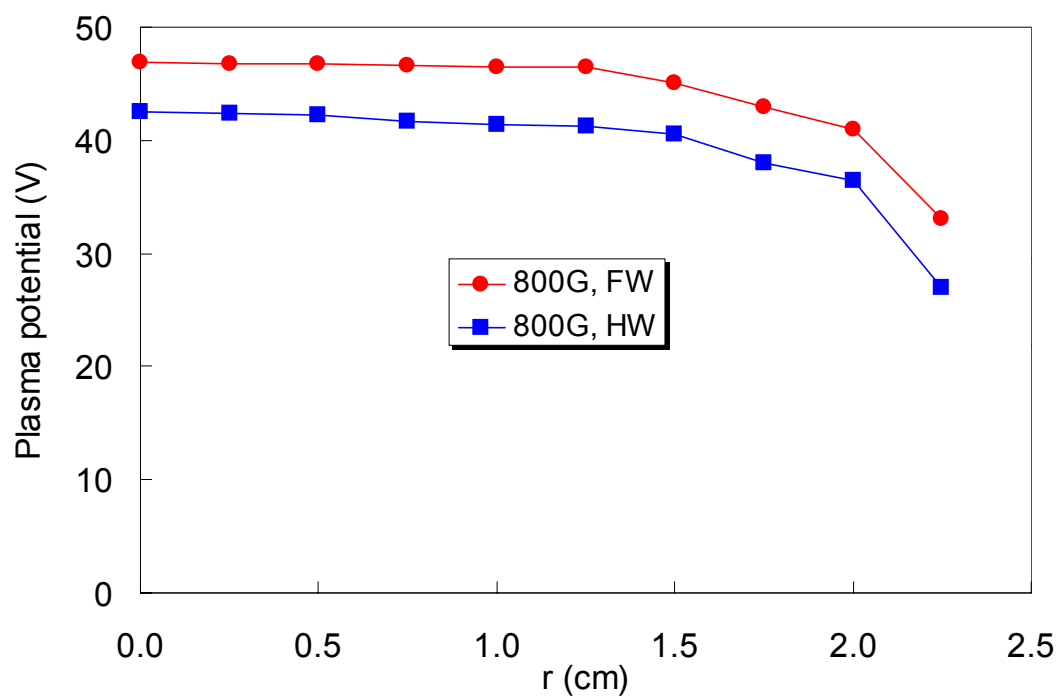


Fig. 21. Plasma potential vs. radius at 800G, $z = 48$ cm for the FW (●) and HW (■) antennas.

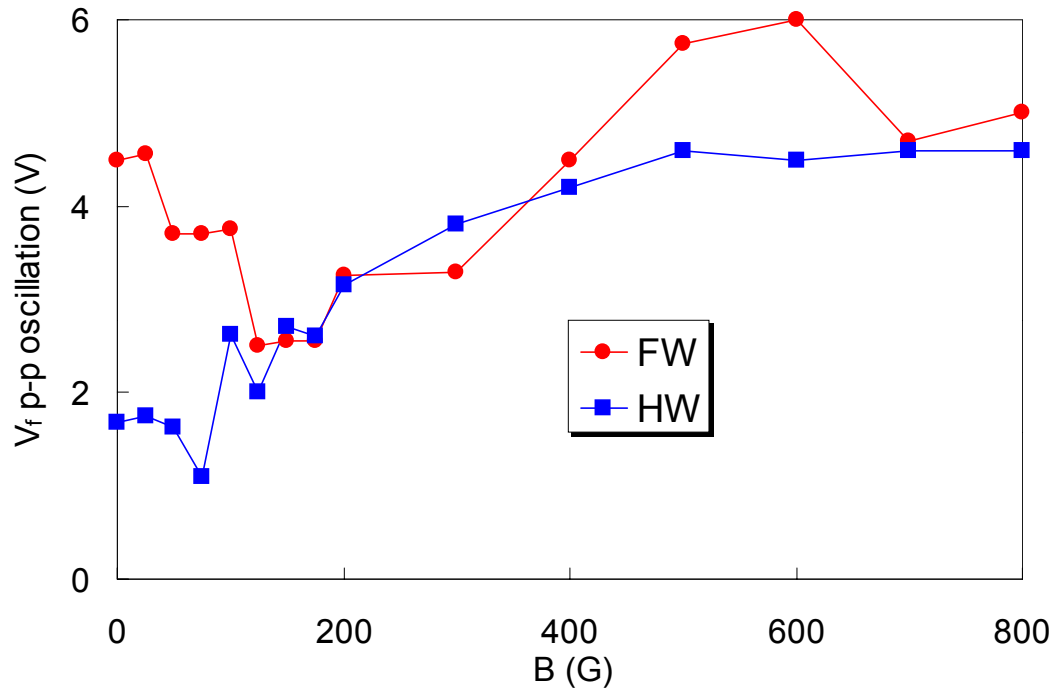


Fig. 22. Peak-to-peak oscillation amplitude in floating potential vs. B_0 at $z = 24$ cm, $r = 1.5$ cm for the two antennas.